Arch. Metall. Mater. **70** (2025), 3, 1095-1100

DOI: https://doi.org/10.24425/amm.2025.154449

DINH VAN CONG[1], SEUNG-YUN SONG[1], DONG-GWAN LEE[1], JIN-CHUN KIM[1*], MINH-THUYET NGUYEN[2], ALEXANDER A. GROMOV[3]

MECHANICAL BEHAVIOR AND MICROSTRUCTURAL EVOLUTION IN 316L STAINLESS STEEL PROCESSED BY LASER POWDER BED FUSION UNDER DIFFERENT ANNEALING CONDITIONS

This study investigates the influence of annealing temperature on the microstructure and mechanical properties of 316L stainless steel manufactured using laser powder bed fusion technology. Higher annealing temperatures reduced porosity in both horizontally and vertically printed samples. Horizontal samples exhibited vertically aligned melting pools, while vertical samples showed scale-like pool structures. Annealing at 950°C dissolved melting pool boundaries and created continuous grain structures, with vertical samples demonstrating faster grain growth. Horizontal samples showed higher initial hardness, but lower ductility than vertical samples. The annealing process improved elongation in all samples, while microstructural analysis revealed that horizontal samples had extensive twinning and dislocation activity.

Keywords: 316L stainless steel; laser powder bed fusion; building direction; heat treatment

1. Introduction

316L stainless steel, an iron-based alloy with chromium, nickel, and molybdenum, is widely used due to its excellent corrosion resistance, mechanical properties, and biocompatibility, supporting applications from marine components to medical implants where durability and safety are essential [1-9]. Traditional methods like forging, casting, and extrusion limit the design possibilities for complex shapes, often requiring additional machining or welding, which increases production time and cost [10,11]. Laser powder bed fusion (LPBF) technology offers a solution by enabling the layer-by-layer construction of complex 3D structures from metallic powders, providing greater design freedom and minimizing material waste compared to conventional methods [12-17]. Achieving the desired material properties with LPBF requires careful optimization of process parameters, including scanning strategy, energy density, and especially printing orientation, as build direction influences the microstructure and mechanical properties due to the directional nature of layer deposition [18-21]. Studies have shown that characteristics like ductility, strength, and surface finish vary between horizontal and vertical build orientations, posing challenges for applications needing isotropic performance. Post-processing techniques, such as annealing, are also crucial for enhancing ductility, stabilizing dimensions, and reducing internal stresses, with the annealing temperature controlling microstructural changes like grain growth and defect reduction, directly affecting hardness and strength [22-25]. This study aims to explore strengthening mechanisms and microstructural evolution of 316L stainless steel produced by LPBF under the impact of annealing temperatures, using tensile and hardness tests on specimens printed in both vertical and horizontal orientations, along with detailed microscopic analyses to clarify structure-property relationships.

2. Experimental

In this study, gas-atomized 316L stainless steel powder, supplied by Oerlikon Metco (USA), was used as the primary material. The alloy composition included 61.15 wt.% Fe, 12 wt.% Ni, 17 wt.% Cr, 2.5 wt.% Mo, 2.3 wt.% Si, 1 wt.% Mn, and 0.03 wt.% C. Tensile samples were fabricated using a Metalsys 120D machine from Winforsys (South Korea) in both horizontal (X-sample) and vertical (Z-sample) orientations relative to the building direction. Printing was conducted with

[1] UNIVERSITY OF ULSAN, SCHOOL OF MATERIALS SCIENCE AND ENGINEERING, ULSAN, REPUBLIC OF KOREA
[2] HANOI UNIVERSITY OF SCIENCE AND TECHNOLOGY, SCHOOL OF MATERIALS SCIENCE AND ENGINEERING, HANOI, VIETNAM
[3] LOMONOSCOV MOSCOW STATE UNIVERSITY, FUNDAMENTAK PHYSIC-CHEMICAL ENGINEERING, MOSCOW, RUSSIA

* Corresponding author:jckimpml@ulsan.ac.kr

consistent parameters: a laser power of 144 W, a scanning speed of 750 mm/s, and a laser diameter of 0.08 mm. The samples, with dimensions of Ø6 mm × 42 mm, and a gauge section of Ø3 mm × 15 mm, were prepared in accordance with ISO 22647. Following fabrication, the samples underwent heat treatment at either 650°C or 950°C for 2 hours, followed by natural cooling inside the furnace.

The microstructure of samples was analyzed using various analytical tools, including scanning electron microscopy (SEM, JEOL JSM-6500F, Japan) an electron backscatter diffraction (EBSD, FE-SEM-S500 equipped with Velocity™ EBSD Camera, Japan), transmission electron microscopy (TEM, JEM-2100, Japan), and X-ray diffraction (XRD, Rigaku Ultima IV, Japan). Hardness measurements were conducted with a Mitutoyo Vickers Hardness tester (MVK-H1, Mitutoyo Co., Ltd, Japan). Tensile testing of both as-built and annealed samples was conducted using an Instron tensile tester (DTU900-MH, South Korea) at a fixed strain rate of 1 mm/min. To ensure accurate results, hardness and tensile strength measurements were repeated five times for each experimental condition.

3. Results and discussion

Fig. 1 presents SEM images capturing the structural evolution of the annealed samples. In the X-samples, post-printing structures manifested as vertically aligned melting pools with elongated boundaries that span the specimen length. In contrast, the Z-samples exhibit a distinct structure characterized by overlapping, scale-like melting pools. Notably, the X-samples show occasional localized overheating, resulting in the extension of melting pools into adjacent layers, a phenomenon absent from the Z-samples. These unique melting pool structures persisted even after annealing at 650°C. However, an increase in annealing temperature to 950°C led to a complete transformation: the melting pool structures were replaced by grain boundaries with different shapes. They also reveal the characteristic cellular structure in both the as-built and 650°C-annealed samples, which were not observed after annealing at 950°C. Significantly, the annealing process at 950°C successfully dissolved the melt-pool boundaries, resulting in a continuous grain structure. In addition, the highest porosity was achieved in the as-built samples, registering roughly 0.2%, and the lowest porosity was achieved in samples annealed at 950°C, where porosity reached approximately 0.05%. These results indicate that higher annealing temperatures lead to density improvement in the samples.

To gain a comprehensive understanding of the microstructure in both as-built and annealed samples, EBSD measurements were conducted, as shown in Fig. 2. The inverse pole figure (IPF) maps reveal that the crystallographic orientation of the iron (Fe) phase is randomly distribution across all samples, with a predominant orientation along the <101> direction. The phase map indicates that all samples are primarily composed of the austenitic (FCC) phase, accounting for approximately 99.9% of the volume. The remaining phases, ferrite (BCC) and hexaferrum (HCP), mainly distribute along grain boundaries. Overall, the annealing process did not significantly alter the crystallographic orientation of the material. In X-samples, the grains grew parallel to the building direction in two distinct morphologies: equiaxed and platelet. The equiaxed grains were substantially larger than the platelet grains. Grains extended beyond melting pool boundaries into adjacent layers, indicative of epitaxial growth. In Z-samples, the grains grew epitaxially but in a zig-zag pattern instead of parallel columns. Grain orientation

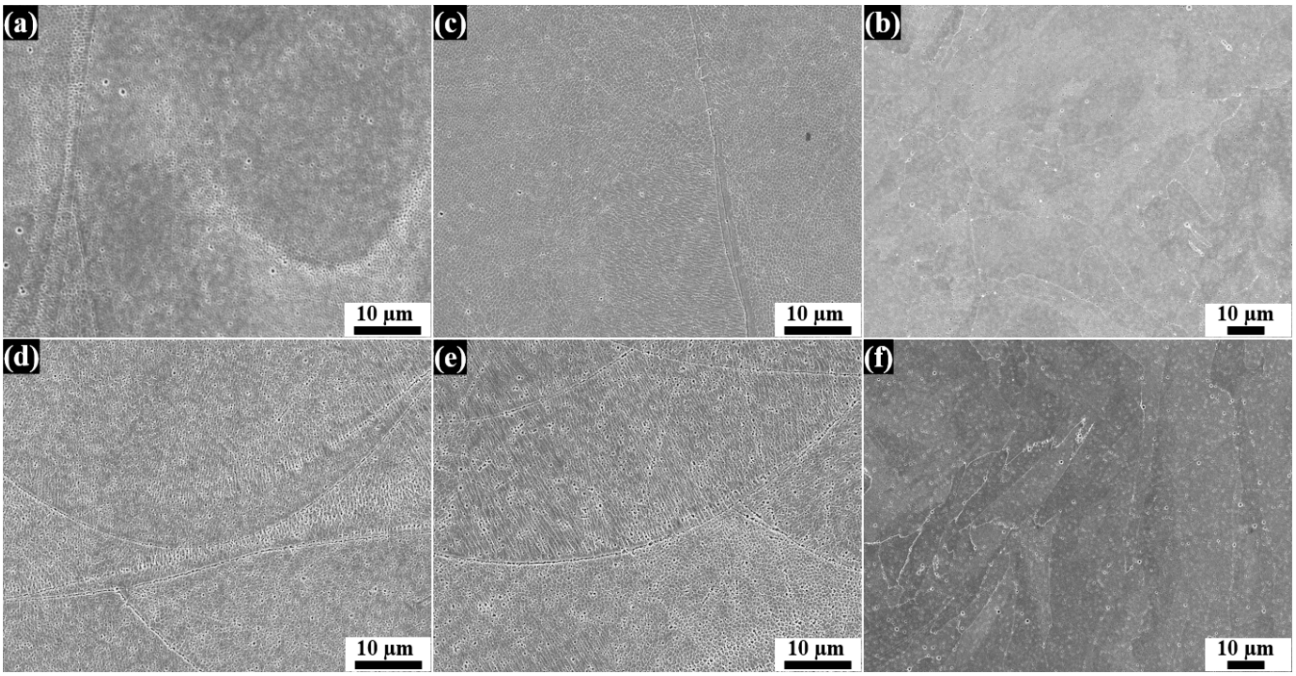

Fig. 1. SEM images of printed 316L stainless steel annealed at different temperatures for 2 hours: X-samples in the (a) as-built state and after (b) 650°C and (c) 950°C annealing and Z-samples in the (d) as-built state and after (e) 650°C and (f) 950°C annealing

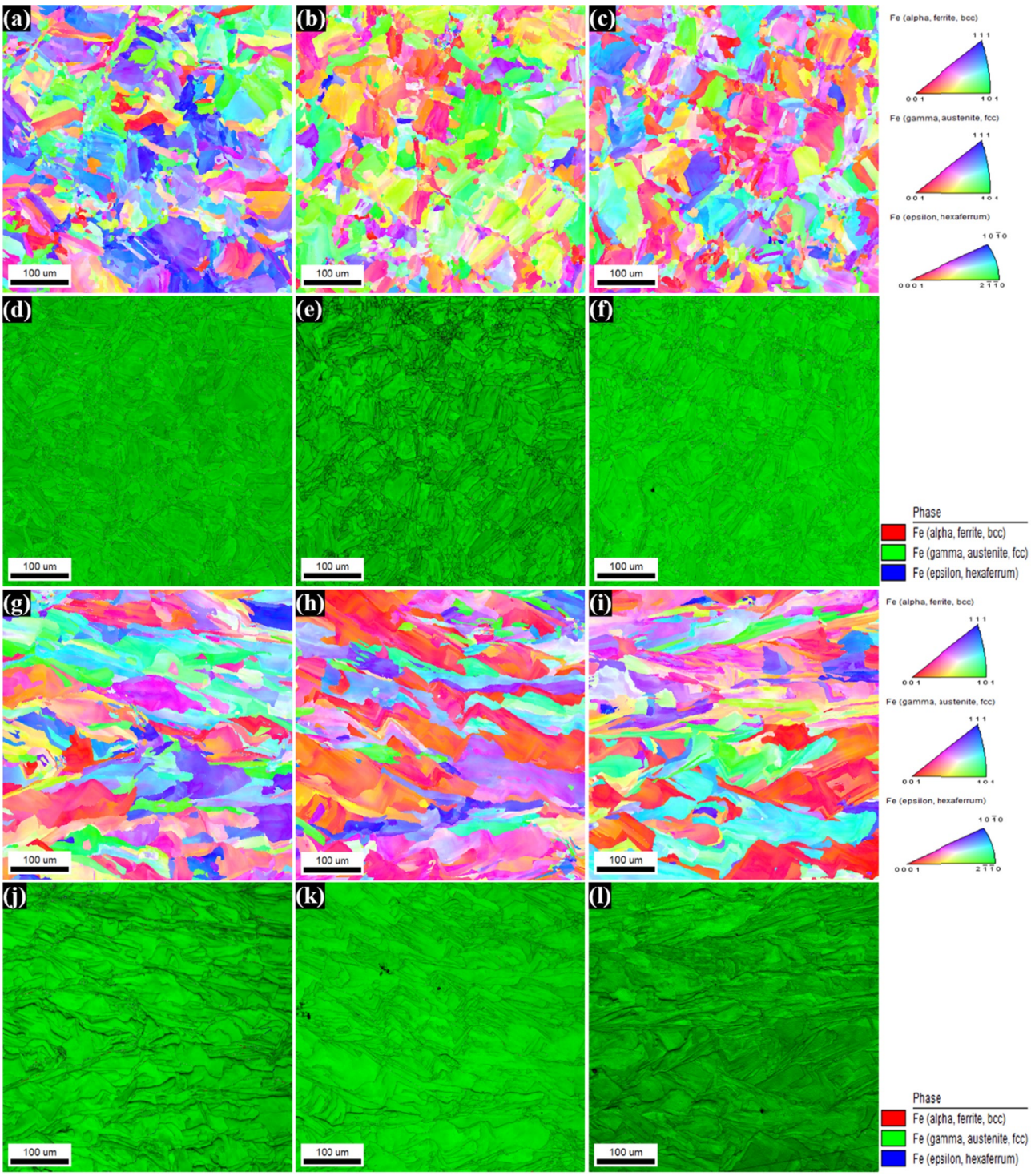

Fig. 2. (a-c, g-i) Inverse pole figure (IPF) and (d-f, j-l) phase maps of printed 316L stainless steel annealed at different temperatures for 2 hours: X-samples in the (a, d) as-built state and after (b, e) 650°C and (c, f) 950°C annealing and Z-samples in the (g, j) as-built state and after (h, k) 650°C and (i, l) 950°C annealing

was maintained across neighboring melt pools within the same layer. However, grain expansion across melt pools was smaller than interlayer expansion, resulting in an elongated morphology. Qualitative analysis indicates that the density of regions with high stress in the X-samples was higher than Z-samples under all annealing conditions. Notably, the twin boundary fraction was smaller, and the high-angle grain boundaries fraction was larger in X-samples compared to Z-samples. These fractions gradually decreased with annealing in both X- and Z-samples. These results demonstrate that X-samples exhibit higher residual stress than Z-samples, due to the multiple thermal cycles and shrinkage stress that occur during rapid melting and solidification. Additionally, the X-samples exhibit average grain sizes of 36.6 µm, 37.6 µm, and 38.7 µm in their as-built state, after annealing at 650°C and 950°C, respectively. The corresponding values for the Z-samples were larger, measuring 62.95 µm, 78.03 µm, and

83.83 μm. This difference underscores the significantly faster grain growth rate in the Z-samples compared to the X-samples. This difference significantly affected the mechanical properties of the material after annealing.

The hardness results are summarized in TABLE 1. The results indicate that the Z-samples exhibit higher hardness than the X-samples, but both orientations experienced a decrease in hardness with increasing annealing temperature. This decline is attributed to grain growth during annealing, which reduces grain boundary strengthening. As grain size increases, fewer boundaries hinder dislocation movement, lowering hardness according to the Hall-Petch relationship.

TABLE 1

Hardness and tensile properties of the tested 316L stainless steel

Condition	Yield strength (MPa)	Ultimate tensile strength (MPa)	Elongation (%)	Hardness (HV)
X-samples				
As-built	681 ± 10	735 ± 7	32 ± 5	217 ± 5
650°C	586 ± 21	689 ± 12	42 ± 4	199 ± 7
950°C	578 ± 15	738 ± 20	49 ± 7	190 ± 3
Z-samples				
As-built	785 ± 12	832 ± 12	49 ± 4	229 ± 6
650°C	533 ± 19	574 ± 10	51 ± 6	211 ± 3
950°C	473 ± 17	609 ± 15	61 ± 5	191 ± 5

The tensile test results are also summarized in TABLE 1, and Fig. 3 illustrates the stress-strain curves for both X- and Z-samples in their as-built and annealed states. In the as-built state, the Z-samples displayed higher strength compared to the X-samples. However, following annealing, the X-samples exhibit higher strength than their Z-sample counterparts. Additionally, the elongation at fracture for the X-samples was consistently lower than that of the Z-samples across all annealing conditions, highlighting the superior ductility of the Z-samples. Moreover, after annealing, the X-samples displayed a higher elastic region than the Z-samples displayed. These distinctions in the tensile properties between X- and Z-direction fabrication may be attributed to factors such as stacking direction and porosity during printing, as reported in previous studies. The X-samples maintained relatively homogeneous mechanical properties due to tight bonding between melting pools (melting tracks) formed during laser processing, resulting in minimal changes in tensile properties after heat treatment. In contrast, the Z-samples formed structures with potential voids and irregular melting boundaries (melting layers), leading to a significant decrease in strength after heat treatment.

Bright-field TEM imaging was performed on the deformation zones of X- and Z-samples after tensile testing, as shown in Fig. 4. The images demonstrate extensive twinning activity in the X-samples. Numerous dislocations and stacking faults between the twin lamella were also observed, likely interacting strongly during plastic deformation. The stacking faults arise from partial dislocations formed via dislocation-twin interactions. Circular- and rectangular-shaped inclusions, approximately 30-100 nm in size, were present in the microstructure of all annealed Z-samples, both within grains and along grain boundaries. These particles were enriched in Si, Al, Mn, and O. Such inclusions may form via reactions between the molten powder and excess oxygen during manufacturing, followed by rapid quenching to an amorphous state. An alternative possibility is that they originate from an oxide layer on the powder feedstock surface [26].

4. Conclusions

This study investigated the relationships between printing orientation, annealing temperature, and properties of LPBF-fabricated 316L stainless steel. The microstructure varied significantly with build orientation: X-samples exhibit elongated melt pools with localized overheating, while Z-samples showed distinctive scale-like structures. Annealing at 950°C dissolved melt-pool boundaries and formed continuous grain structures.

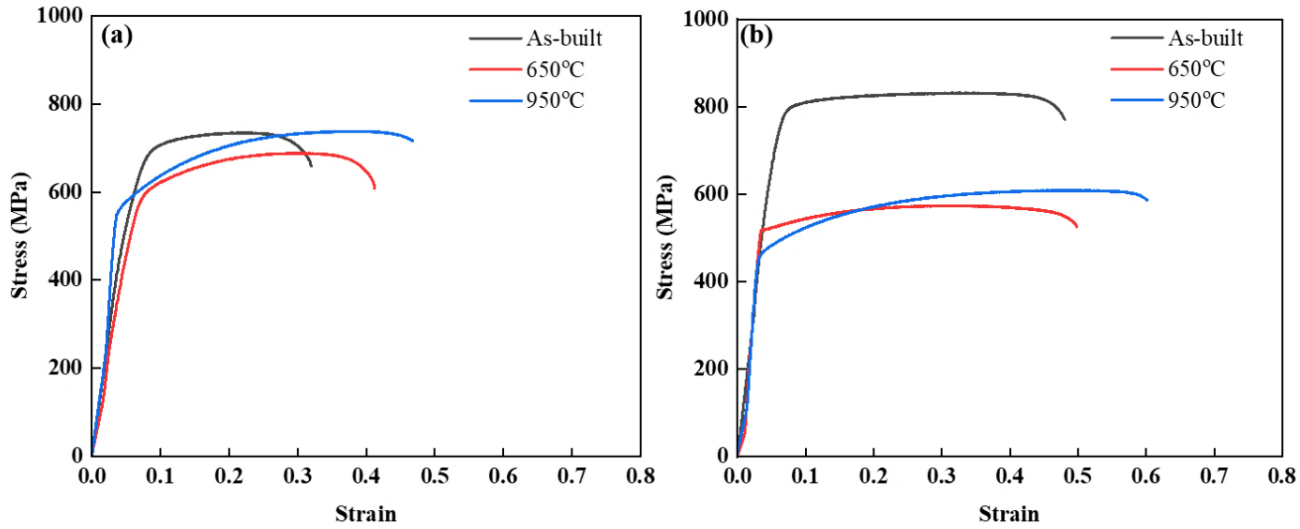

Fig. 3. Stress-strain curves for (a) X- and (b) Z-samples (also refer to TABLE 2)

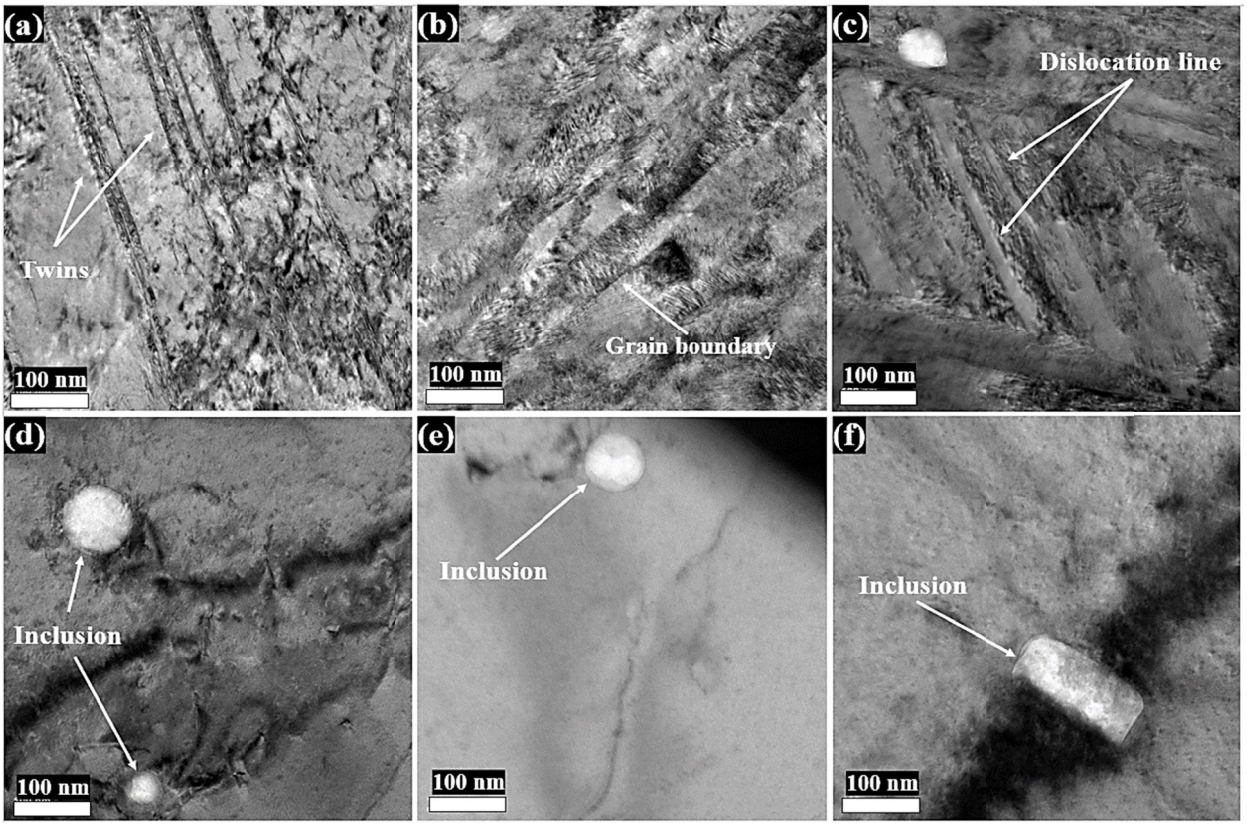

Fig. 4. TEM bright-field images of the tensile test samples in deformation regions: X-samples in the (a) as-built state and after annealing at (b) 650°C and (c) 950°C for 2 hours and Z-samples in the (d) as-built state and after annealing at (e) 650°C and (f) 950°C for 2 hours

Mechanical properties were strongly influenced by both build orientation and heat treatment. Initially, Z-samples showed higher hardness and ductility, but lower strength compared to X-samples. After annealing, X-samples demonstrate increased strength, while both orientations experienced decreased hardness. Additionally, TEM analysis identified Si, Al, Mn, and O-rich inclusions, indicating reactions between molten powder and oxygen. These findings provide valuable insights for optimizing 316L properties in LPBF applications.

Acknowledgement

This work was supported by the Technology Program No.20024344, Development of Al-based high carbon steel alloy design and sintering-based additive manufacturing technology for 7.0L/Hr-level high-speed production of powertrain components with tensile strength over 1.0 Gpa in the next-generation mobility. It was also supported by "Regional Innovation Strategy (RIS)" through the National Research Foundation of Korea (NRF), funded by the Ministry of Education (MOE)(2021RIS-003).

REFERENCES

[1] A. Di Schino, Manufacturing and Applications of Stainless Steels. Met. **10**, 327 (2020). DOI: https://doi.org/10.3390/MET10030327

[2] G.A. Barragan, F. Mariani, R.T. Coelho, Application of 316L Stainless Steel Coating by Directed Energy Deposition Process. IOP Conf. Ser. Mater. Sci. Eng. **1154**, 012014 (2021). DOI: https://doi.org/10.1088/1757-899x/1154/1/012014

[3] M. Saravanan, A. Devaraju, N. Venkateshwaran, A. Krishnakumari, J. Saarvesh, A Review on Recent Progress in Coatings on AISI Austenitic Stainless Steel. Mater. Today Proc. **5**, 14392-14396 (2018). DOI: https://doi.org/10.1016/j.matpr.2018.03.024

[4] A. Francis, Y. Yang, S. Virtanen, A.R. Boccaccini, Iron and Iron-Based Alloys for Temporary Cardiovascular Applications. J. Mater. Sci. Mater. Med. **26**, 1-16 (2015). DOI: https://doi.org/10.1007/S10856-015-5473-8

[5] V.B. Vukkum, R.K. Gupta, Review on Corrosion Performance of Laser Powder-Bed Fusion Printed 316L Stainless Steel: Effect of Processing Parameters, Manufacturing Defects, Post-Processing, Feedstock, and Microstructure. Mater. Des. **221**, 110874 (2022). DOI: https://doi.org/10.1016/j.matdes.2022.110874

[6] M.J.K. Lodhi, K.M. Deen, M.C. Greenlee-Wacker, W. Haider, Additively Manufactured 316L Stainless Steel with Improved Corrosion Resistance and Biological Response for Biomedical Applications. Addit. Manuf. **27**, 8-19 (2019). DOI: https://doi.org/10.1016/j.addma.2019.02.005

[7] N.S. Al-Mamun, K. Mairaj Deen, W. Haider, E. Asselin, I. Shabib, Corrosion Behavior and Biocompatibility of Additively Manufactured 316L Stainless Steel in A Physiological Environment: The Effect of Citrate Ions. Addit. Manuf. **34**, 101237 (2020). DOI: https://doi.org/10.1016/j.addma.2020.101237

[8] J. Zhao, Z. Zhai, D. Sun, C. Yang, X. Zhang, N. Huang, X. Jiang, K. Yang, Antibacterial Durability and Biocompatibility of Antibacterial-Passivated 316L Stainless Steel in Simulated Physiological Environment. Mater. Sci. Eng. C **100**, 396-410 (2019). DOI: https://doi.org/10.1016/j.msec.2019.03.021

[9] M. Venkatraman, K. Pavitra, V. Jana, T. Kachwala, Manufacturing and Critical Applications of Stainless Steel – An Overview. Adv. Mat. Res. **794**, 163-173 (2013). DOI: https://doi.org/10.4028/www.scientific.net/amr.794.163

[10] F. Bartolomeu, M. Buciumeanu, E. Pinto, N. Alves, O. Carvalho, F.S. Silva, G. Miranda, 316L Stainless Steel Mechanical and Tribological Behavior – A Comparison Between Selective Laser Melting, Hot Pressing and Conventional Casting. Addit. Manuf. **16**, 81-89 (2017). DOI: https://doi.org/10.1016/j.addma.2017.05.007

[11] J.R.J. Michla, R. Nagarajan, S. Krishnasamy, S. Siengchin, S.O. Ismail, T.R. Prabhu, Conventional and Additively Manufactured Stainless Steels: A Review. Trans. Indian Inst. Met. **74**, 1261-1278 (2021). DOI: https://doi.org/10.1007/S12666-021-02305-7

[12] P.A. Kuznetsov, A.A. Zisman, S.N. Petrov, I.S. Goncharov, Structure and Mechanical Properties of Austenitic 316L Steel Produced by Selective Laser Melting. Russ. Metall. **2016**, 930-934 (2016). DOI: https://doi.org/10.1134/S0036029516100104

[13] D. Riabov, A. Leicht, J. Ahlström, E. Hryha, Investigation of The Strengthening Mechanism in 316L Stainless Steel Produced with Laser Powder Bed Fusion. Mater. Sci. Eng. A. **822**, 141699 (2021). DOI: https://doi.org/10.1016/j.msea.2021.141699

[14] M. Khorasani, A.H. Ghasemi, U.S. Awan, S. Singamneni, G. Littlefair, E. Farabi, M. Leary, I. Gibson, J.K. Veetil, B. Rolfe, On the Role of Process Parameters on Meltpool Temperature and Tensile Properties of Stainless Steel 316L Produced by Powder Bed Fusion. J. Mater. Res. Technol. **12**, 2438–2452 (2021). DOI: https://doi.org/10.1016/j.jmrt.2021.04.043

[15] C.Y. Yap, C.K. Chua, Z.L. Dong, Z.H. Liu, D.Q. Zhang, L.E. Loh, S.L. Sing, Review of Selective Laser Melting: Materials and Applications. Appl. Phys. Rev. **2**, 041101 (2015). DOI: https://doi.org/10.1063/1.4935926

[16] S.Y. Song, D.W. Lee, D.V. Cong, J.W. Kim, S.M. Lee, S.H. Joo, J.C. Kim, Microstructural Analysis of STS316L Samples Manufactured by Powder Bed Fusion and Post-Heat Treatments. J. Powder Mater. Inst. **29**, 14-21 (2022). DOI: https://doi.org/10.4150/kpmi.2022.29.1.14

[17] Y. Huang, H.J. Ryu, K.-A. Lee, Effect of Hatch Spacing on The Microstructure and Mechanical Properties of SA508 Gr.3 Steel Fabricated by Laser Powder Bed Fusion. J. Powder Mater. Inst. **32**, 50-58 (2025). DOI: https://doi.org/10.4150/jpm.2024.00479

[18] N. Jin, Z. Yan, Y. Wang, H. Cheng, H. Zhang, Effects of Heat Treatment on Microstructure and Mechanical Properties of Selective Laser Melted Ti-6Al-4V Lattice Materials. Int. J. Mech. Sci. **190**, 106042 (2021). DOI: https://doi.org/10.1016/j.ijmecsci.2020.106042

[19] J.M. Park, E.S. Kim, H. Kwon, P. Sathiyamoorthi, K.T. Kim, J.H. Yu, H.S. Kim, Effect of Heat Treatment on Microstructural Heterogeneity and Mechanical Properties of 1%C-CoCrFeMnNi Alloy Fabricated by Selective Laser Melting. Addit. Manuf. **47**, 102283 (2021). DOI: https://doi.org/10.1016/j.addma.2021.102283

[20] M.T. Nguyen, H.V. Nguyen, T.H. Le, Q.K. Dang, J.C. Kim, Properties of the Interface between the As-Built Ti 6Al 4V sample and the Ti Substrate in Selective Laser Sintering. Int. J. Mod. Phys. B **34**, 2040137 (2020). DOI: https://doi.org/10.1142/S0217979220401372

[21] A. Mertens, S. Reginster, H. Paydas, Q. Contrepois, T. Dormal, O. Lemaire, J. Lecomte-Beckers, Mechanical Properties of Alloy Ti-6Al-4V and of Stainless Steel 316L Processed by Selective Laser Melting: Influence of Out-Of-Equilibrium Microstructures. Powder Metall. **57**, 184-189 (2014). DOI: https://doi.org/10.1179/1743290114Y.0000000092

[22] C. Gao, Z. Liu, Z. Xiao, W. Zhang, K. Wong, A.H. Akbarzadeh, Effect of Heat Treatment on SLM-Fabricated TiN/AlSi10Mg Composites: Microstructural Evolution and Mechanical Properties. J. Alloys Compd. **853**, 157722 (2021). DOI: https://doi.org/10.1016/j.jallcom.2020.156722

[23] W. Li, S. Li, J. Liu, A. Zhang, Y. Zhou, Q. Wei, C. Yan, Y. Shi, Effect of Heat Treatment on AlSi10Mg Alloy Fabricated by Selective Laser Melting: Microstructure Evolution, Mechanical Properties and Fracture Mechanism. Mater. Sci. Eng. A. **663**, 116-125 (2016). DOI: https://doi.org/10.1016/j.msea.2016.03.088

[24] A. Polishetty, G. Littlefair, Heat Treatment Effect on the Fatigue Characteristics of Additive Manufactured Stainless Steel 316L. Int. J. Mater. Mech. Manuf. **7**, 114-118 (2019). DOI: https://doi.org/10.18178/ijmmm.2019.7.2.442

[25] W.S. Shin, B. Son, W. Song, H. Sohn, H. Jang, Y.J. Kim, C. Park, Heat Treatment Effect on The Microstructure, Mechanical Properties, and Wear Behaviors of Stainless Steel 316L Prepared via Selective Laser Melting. Mater. Sci. Eng. A. **806**, 140805 (2021). DOI: https://doi.org/10.1016/j.msea.2021.140805

[26] P. Krakhmalev, G. Fredriksson, K. Svensson, I. Yadroitsev, I. Yadroitsava, M. Thuvander, R. Peng, Microstructure, Solidification Texture, and Thermal Stability of 316L Stainless Steel Manufactured by Laser Powder Bed Fusion. Met. **8**, 643 (2018). DOI: https://doi.org/10.3390/met8080643